Spatially resolved edge currents and guided-wave electronic states in graphene

M. T. Allen[1], O. Shtanko[2], I. C. Fulga[3], A. R. Akhmerov[4], K. Watanabe[5], T. Taniguchi[5], P. Jarillo-Herrero[2], L. S. Levitov[2] and A. Yacoby[1]*

Exploiting the light-like properties of carriers in graphene could allow extreme non-classical forms of electronic transport to be realized[1-8]. In this vein, finding ways to confine and direct electronic waves through nanoscale streams and streamlets, unimpeded by the presence of other carriers, has remained a grand challenge[9-12]. Inspired by guiding of light in fibre optics, here we demonstrate a route to engineer such a flow of electrons using a technique for mapping currents at submicron scales. We employ real-space imaging of current flow in graphene to provide direct evidence of the confinement of electron waves at the edges of a graphene crystal near charge neutrality. This is achieved by using superconducting interferometry in a graphene Josephson junction and reconstructing the spatial structure of conducting pathways using Fourier methods[13]. The observed edge currents arise from coherent guided-wave states, confined to the edge by band bending and transmitted as plane waves. As an electronic analogue of photon guiding in optical fibres, the observed states afford non-classical means for information transduction and processing at the nanoscale.

Electrons in Dirac materials such as graphene can be manipulated using external fields that control electron refraction and transmission in the same way that lenses and optical elements manipulate light[1,2,6,7]. Several of the key ingredients, including phase-coherent Klein transmission and reflection[3-5], ballistic transport[8] and transverse focusing on micrometre scales[14], have already been established. One promising yet unexplored direction, which we investigate here, is the quasi-one-dimensional confinement of electrons in direct analogy to refraction-based confinement of photons in optical fibres. Electronic guided modes formed by a line gate potential, although discussed in the literature[9-12], have so far evaded direct experimental realization. Extending the fibre-optic techniques to the electronic domain is key to achieving control of electron waves at a level comparable to that for light in optical communication systems.

Rather than pursuing the schemes discussed in refs 9–12, here we explore modes at the graphene edges. The atomically sharp graphene edges provide a natural vehicle for band bending near the boundary, which then confines the electronic waves in the direction transverse to the edge. The resulting guided 'fibre-optic' modes are situated outside the Dirac continuum (see Fig. 1a,b), propagating along the crystal edge as plane waves and decaying into the bulk as evanescent waves. This approach to carrier guiding is particularly appealing because of the ease with which band bending at the graphene edge can be realized, as well as because there is

no threshold for fibre-optic states to occur: they are induced by an edge potential of either sign, positive or negative, no matter how weak (see discussion below and in the Supplementary Methods). The presence of such guided modes enhances the density of current-carrying states at the edge. The effects of electron confinement and guiding are strongest near charge neutrality, where the edge potential is unscreened, whereas uniform behaviour is recovered away from neutrality (see Fig. 1c and Supplementary Fig. 1).

The edge currents associated with guided states, anticipated at zero magnetic field, have so far eluded experimental detection owing to the challenge of imaging current with submicron spatial resolution. In particular, scanning tunnelling spectroscopy (STS) images the density of states but not the current flow[15,16], whereas macroscopic conductivity cannot distinguish the edge and bulk contributions[17,18]. With this motivation, we developed a technique to spatially image electric current pathways and applied it to high-mobility graphene. We employ superconducting quantum interferometry in a graphene Josephson junction to reconstruct the spatial structure of the electronic states which transmit supercurrent, which allows edge and bulk contributions to be disentangled[13,19].

Our approach employs gated Josephson junctions consisting of graphene coupled to superconducting titanium/aluminium electrodes (Fig. 1d). A gate electrode is used to tune the carrier density, n, in the graphene. To access the intrinsic properties of graphene at densities near charge neutrality, flakes are isolated from substrate-induced disorder through placement on thin hexagonal boron nitride (hBN) substrates[20]. A total of four bilayer devices and one monolayer device are investigated, BL1, BL2, BL3, BL4 and ML1, all of which exhibit similar behaviour (Supplementary Table 1). Measurements of the a.c. voltage drop dV across the junction in response to an a.c. current modulation dI were conducted using lock-in techniques in a dilution refrigerator at 10 mK, well below the critical temperature of Al. Figure 1e–h shows transport data from one of the bilayer devices. On sweeping the d.c. current bias $I_{d.c.}$, a sharp transition in resistance between dissipationless and normal metal behaviour appears at a critical current I_c, a transport signature of the Josephson effect (Fig. 1e,f).

We obtain real-space information by applying a magnetic flux Φ through the junction area, which induces a position-dependent superconducting phase difference parallel to the graphene/contact interface[21]. As a result, the critical current I_c exhibits interference fringes in the magnetic field B (Fig. 1e). The measured interference patterns feature well-defined nodes, which indicates the absence of field inhomogeneity such as that due to vortices[22]. The critical current I_c can be expressed as the magnitude of the complex Fourier

[1]Department of Physics, Harvard University, Cambridge, Massachusetts 02138, USA. [2]Department of Physics, Massachusetts Institute of Technology, Cambridge, Massachusetts 02139, USA. [3]Department of Condensed Matter Physics, Weizmann Institute of Science, Rehovot 76100, Israel. [4]Kavli Institute of Nanoscience, Delft University of Technology, Lorentzweg 1, 2628 CJ Delft, The Netherlands. [5]Environment and Energy Materials Division, National Institute for Materials Science, 1-1 Namiki, Tsukuba, Ibaraki 305-0044, Japan. *e-mail: yacoby@physics.harvard.edu
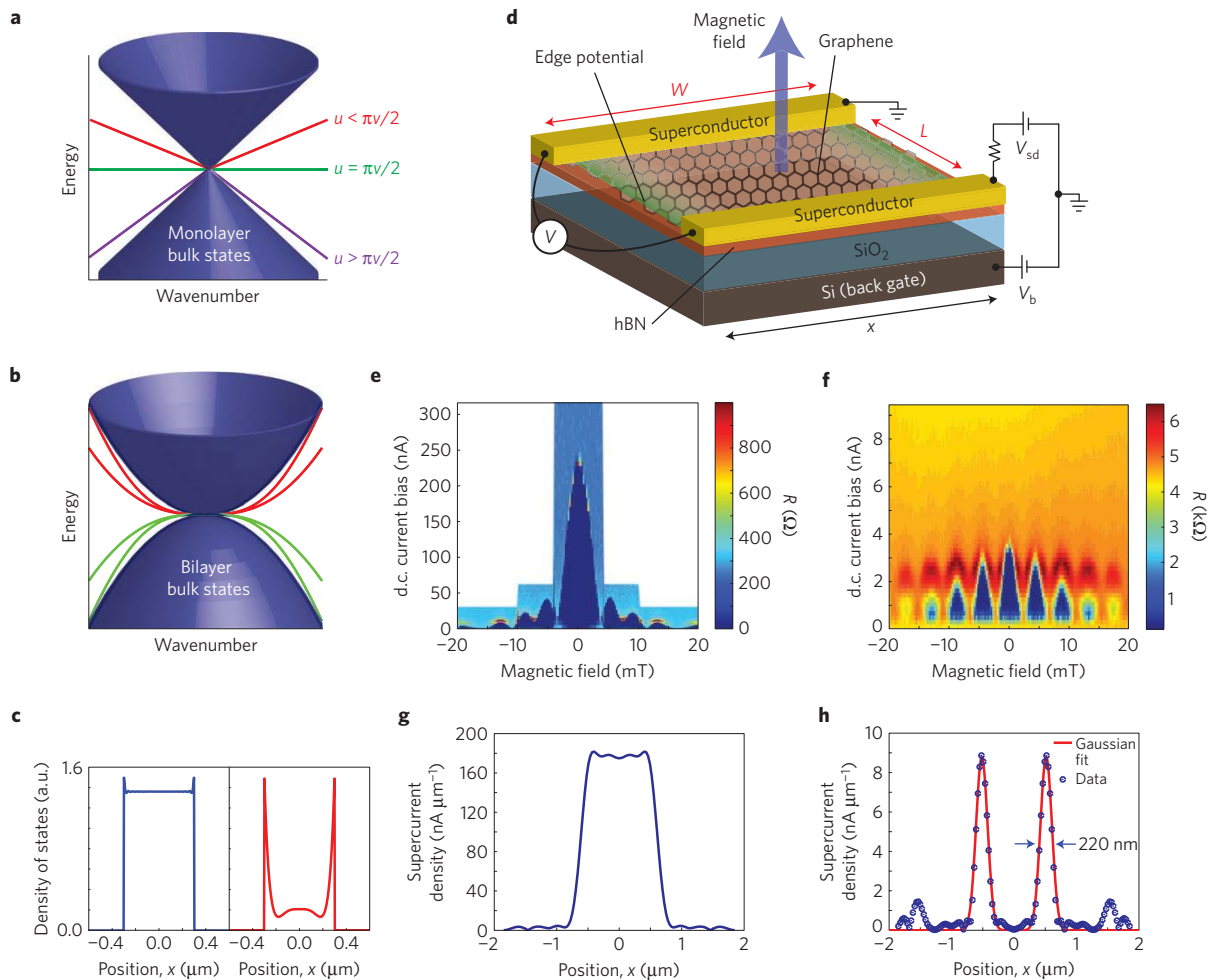
Figure 1 | 'Fibre-optic' modes and spatially resolved current imaging in a graphene Josephson junction. a,b, Guided edge modes induced by an intrinsic band bending near crystal boundary, for monolayer and bilayer graphene (schematic), respectively. Mode frequencies positioned outside the Dirac continuum ensure mode decoupling from the bulk states. Guided modes exist for any edge potential no matter how weak. In a monolayer, mode velocity alternates in sign as the potential strength increases, see equation (5). In a bilayer, the modes occur in pairs (green and red curves: dispersion for positive and negative potential strength, respectively). **c**, The guided modes are manifested through peaks in the density of current-carrying states at the crystal boundaries, prominent near charge neutrality (monolayer graphene, red: $n = 0.05 \times 10^{11}$ cm^{-2}; blue: $n = 2.5 \times 10^{11}$ cm^{-2}). **d**, Schematics of superconducting interferometry in a graphene Josephson junction, which is used to image the spatial structure of current-carrying states. A flux is threaded through the junction area to produce interference patterns, as current bias V_{sd} is applied through the superconducting electrodes and the voltage drop across the device is recorded. Carrier density n is tuned by a gate voltage V_b. **e,f**, The recorded interference pattern is of a single-slit Fraunhofer type at high carrier density, turning into a two-slit SQUID-like interference near neutrality (device $BL1$). **g,h**, Current flow, extracted from the interference data using Fourier techniques, is uniform at high carrier density (**g**) and peaks at the crystal edges for carrier density close to neutrality (**h**).

transform of the current density distribution $J(x)$, providing a simple and concise description of our system. That is, $I_c = |\mathcal{I}_c(B)|$, where

$$\mathcal{I}_c(B) = \int_{-W/2}^{W/2} J(x) e^{2\pi i L B x / \Phi_0} dx \qquad (1)$$

where $\Phi_0 = h/2e$ is the flux quantum, h is Planck's constant, e is the elementary charge, W is the width of the flake (Fig. 1d). Here, following the conventional treatment for wide junctions such that $L \ll W$, where L is the distance between contacts, we ignore the y dependence. The spatial distribution of supercurrent thus dictates the shape of the interference pattern[13,21,23].

The results obtained with this technique show strikingly different behaviour at high and low carrier densities. We observe the conventional uniform-current behaviour at high density, $I_c(B)/I_c(0) \sim |\sin(\pi\Phi/\Phi_0)/(\pi\Phi/\Phi_0)|$, which mimics single-slit Fraunhofer diffraction (Fig. 1e). Defining features of such interference include a central lobe of width $2\Phi_0$ and side lobes with

period Φ_0 and amplitude decaying as $1/B$. However, near the Dirac point, our results exhibit a striking departure from this picture and show a two-slit 'SQUID-like' interference (Fig. 1f)[24]. Such behaviour arises when supercurrent is confined to edge channels and is characterized by slowly decaying sinusoidal oscillations of period Φ_0. Importantly, these two regimes are easily distinguishable without much analysis by the width of the central lobe, which is twice as wide for the uniform case as for the case of edge flow.

The real-space current distribution can be obtained by inverting the relation in equation (1) with the help of the Fourier techniques of Dynes and Fulton[13] (see Supplementary Methods). The resulting current density map reveals strong confinement of supercurrent to the edges of the crystal near the Dirac point (Fig. 1h), a robust experimental feature seen in all five devices. The width of the edge channel, extracted quantitatively from Gaussian fits, is of the order of the electron wavelength ($\sim$200 nm) and consistent across multiple samples. This value is probably an upper bound because the peak width is manifested in the decay envelope of the interference pattern;
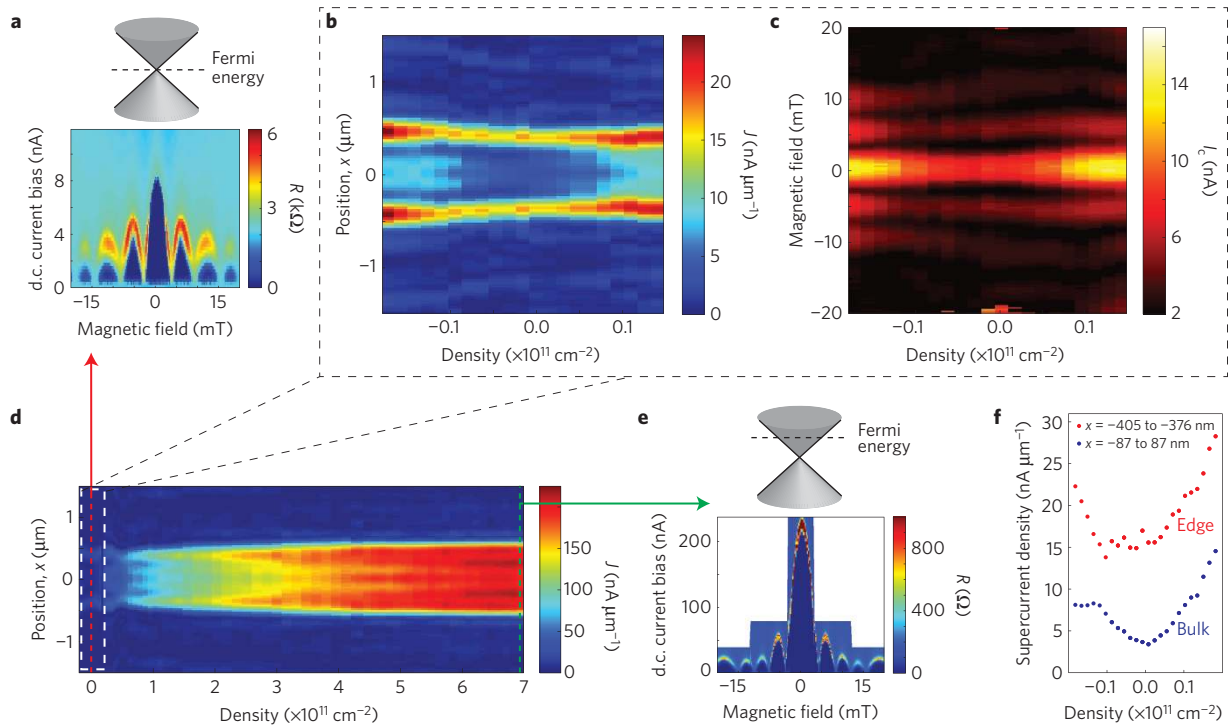
Figure 2 | Gate-tunable evolution of edge and bulk current-carrying states in monolayer graphene. a, Edge-dominated SQUID-like interference pattern at neutrality in device $ML1$ ($n = 2.38 \times 10^9$ cm^{-2}). **b**, Real-space image of current flow confined to the boundaries over a range of densities near neutrality. **c**, The raw interference data corresponding to **b**, taken from the white box in **d**. **d**, A real-space map of current flow as a function of electron concentration reveals the coexistence of edge and bulk modes at intermediate densities. Over the entire scan, the full range of carrier modulation extends into the high 10^{11} range cm^{-2}. **e**, Conventional Fraunhofer pattern for uniform-current flow at high electron density ($n = 7 \times 10^{11}$ cm^{-2}). **f**, Comparison of current amplitudes along the edge (red) and bulk (blue) from the plot in **c**. Current flow is edge-dominated near neutrality. Note that minima for both contributions coincide in n, indicating that a positional edge/bulk density offset is not present.

external factors that suppress the critical current amplitude at high B, such as thermal activation of quasiparticles and suppression of the Al superconducting gap, may also contribute to peak broadening. At high electron density, a conventional Fraunhofer-like behaviour is recovered (Fig. 1e), suggesting a uniform distribution of supercurrent (Fig. 1g). A more numerically expensive Bayesian estimation of the current distribution produces current maps and standard error estimates that agree with the Fourier techniques (see Supplementary Methods and Supplementary Fig. 2).

By tuning carrier concentration with a gate electrode, our measurements reveal coexistence of edge and bulk modes at intermediate densities. This is illustrated in Fig. 2, for a monolayer graphene device. The SQUID-like quantum interference at charge neutrality, which is similar to that for bilayer graphene in Fig. 1, gives the spatial image of supercurrent that confirms edge-dominated transport (Fig. 2a–c,f). As density is increased, bulk current flow increases monotonically and crosses over to mostly uniform flow across the sample (Fig. 2d), signified by conventional Fraunhofer-like interference at high electron density (Fig. 2e). To track the evolution of edge and bulk currents with density, line cuts of the corresponding contributions are provided in Fig. 2f. Notably, the gate voltage corresponding to the charge neutrality point, identified as a dip in the current amplitude for edge and bulk, appear at similar carrier density values, which indicates the absence of edge doping in our system.

Similarly, we systematically explore the interplay between edge and bulk flow in bilayer graphene (Fig. 3). As the Fermi energy approaches the Dirac point from the hole side, the bulk contribution is suppressed faster than the edge contribution, leading to emergence of robust edge currents near zero carrier density (Fig. 3a,b). In this device, current distributions are not plotted at the immediate Dirac point owing to suppression of proximity-induced superconductivity

at high normal state resistances. We note that the range in hole density over which the bulk contribution is recovered varies in different devices. Further, application of an interlayer electric field E breaks crystal inversion symmetry and induces a bandgap[25,26], manifested as a gate-tunable insulating state at the Dirac point (Fig. 3c,d). In this regime, conductance is mediated by edge currents that enclose the bulk, even in the presence of a field-induced gap (Fig. 3e,f).

In both the monolayer and the bilayer cases, raw interference near the Dirac point and at high electron concentration exhibit the salient features that distinguish edge-dominated from bulk-dominated transport, including a width of ϕ_0 versus $2\phi_0$ of the central lobe, as well as Gaussian versus $1/B$ decay of the lobe amplitudes for low and high densities, respectively.

As a simple model of electronic fibre-optic states we consider massless Dirac particles in graphene monolayer in the presence of a line potential:

$$H = v\boldsymbol{\sigma} \cdot \mathbf{p} + V(x) \qquad (2)$$

where $\mathbf{p}$ is momentum, σ_i are pseudospin Pauli matrices and $v \approx 10^6$ m s^{-1}. We seek plane-wave solutions of the Schrödinger equation, $\psi(x, y) = e^{iky}\phi(x)$, where k is the wavevector component along the line and $\phi(x)$ is a two-component spinor wavefunction depending on the transverse coordinate. This problem can be tackled by a matrix gauge transformation $\psi(x) = U(x)\tilde{\psi}(x)$, which eliminates the potential $V(x)$ and generates a mass term in the Dirac equation. Namely, $U(x) = e^{-i\theta(x)\sigma_x}$, with $\theta(x) = (1/\hbar v) \int_0^x V(x')dx'$, yields

$$\tilde{H} = U^{-1}(x)HU(x)$$
$$= \hbar v[-i\sigma_x \partial_x + k\sigma_y \cos 2\theta(x) - k\sigma_z \sin 2\theta(x)] \qquad (3)$$
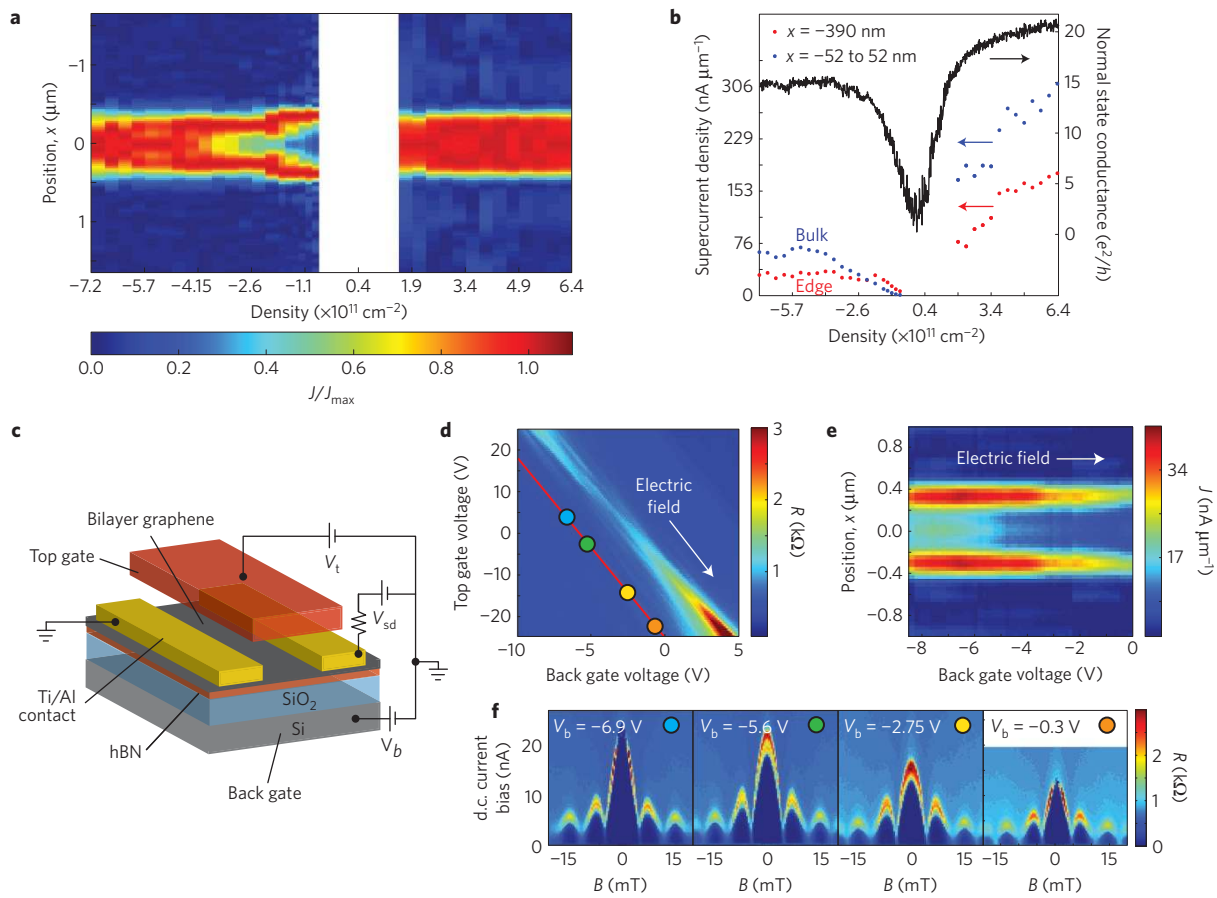
Figure 3 | Edge and bulk currents in bilayer graphene with and without transverse electric field. a, Spatially resolved supercurrent map in device *BL2*, in a normalized plot of $J(x)/J_{max}(x)$. Edge-dominated transport occurs near charge neutrality, whereas an increasing bulk contribution is tuned with carrier concentration. **b**, Comparison of current amplitudes along the edge (red) and through the bulk (blue) from **a**. Enhanced edge currents are prominent at neutrality, whereas a uniformly distributed flow is recovered at high densities. The normal state conductance $G(e^2/h)$ versus carrier density is also shown (black). **c**, Measurement schematic for superconducting interferometry in a dual-gated bilayer graphene Josephson junction. A dual-gated device consists of a bilayer graphene flake on hBN with a suspended top gate, where application of voltages V_t and V_b on the top and back gates enables independent control of the transverse electric field E and carrier density n. **d**, Resistance map as a function of V_b and V_t for bilayer *BL4*. Enhanced resistance at high E fields indicates the emergence of a gate-tunable insulating state due to broken crystal inversion symmetry. **e**, Spatially resolved boundary currents as a function of E field. The vertical axis is a trace along the red path labelled in **b**. **f**, Sequence of Fraunhofer measurements at various locations on the current map in **e**.

As a simple example, we consider the case of an armchair edge, for which the problem on a half plane for carriers in valleys K and K' is equivalent to the problem on a full plane for a single valley. Applying the above method to a potential localized in an interval $-d < x < d$ and focusing on the long-wavelength modes such that $kd \ll 1$, we can use a step approximation $\theta(x) \approx (u/2v)\,\text{sgn}(x)$ with the parameter $u = (1/\hbar) \int_{-d}^{d} V(x')\,dx'$. We arrive at the seminal Jackiw–Rebbi problem for a Dirac equation with a mass kink

$$\tilde{H} = \hbar v(-i\sigma_x\partial_x + \sigma_y\tilde{k} + \sigma_z m(x)) \qquad (4)$$

where $\tilde{k} = k\cos(u/v)$, $m(x) = -k\sin(u/v)\,\text{sgn}(x)$. This problem can be solved directly and explicitly[27], yielding guided-wave states as products of the zero-mode state found from $\tilde{H}$ for $\tilde{k} = 0$ and the plane-wave factors e^{iky}. The energies of these states are simply $\epsilon = \eta\hbar v\tilde{k}$ with the sign $\eta = \text{sgn}(m(0^+) - m(0^-))$. This gives a linear dispersion $\epsilon = \hbar\tilde{v}|k|$, with the velocity

$$\tilde{v} = v\cos(u/v)\text{sgn}(\sin(u/v)) \qquad (5)$$

As $|\tilde{v}| < v$, for each k the energies of these states lie outside the bulk continuum $|\epsilon| \geq \hbar v|k|$ (see Fig. 1a). Decoupling from the bulk

states ensures confinement to the region near the $x = 0$ line. The connection with the theory of zero modes renders robustness to our confinement mechanism. Similar guided-wave states are obtained for an edge potential in graphene bilayer (see Fig. 1b).

In Fig. 4, we compare supercurrent density measurements with a theoretical prediction for density of states. Current density traces $J(x)$ measured in the bilayer device *BL3* at different densities have a strong edge component near neutrality, gradually evolving to the bulk flow away from neutrality. Traces of the density of states, obtained from the above model, exhibit qualitatively similar behaviour (Fig. 4b). For the simulation, a delta function potential approximation was used with the best-fit value $\hbar u = 0.7$ eV nm (see Supplementary Methods).

Another key feature borne out by the above model is the robustness of the guided states in the presence of edge disorder. Indeed, as the length scales defined by the evanescent waves are of the order of electron wavelength λ, the resulting modes are weakly confined to the edge at low carrier density. Such modes tend to decouple from the short-range edge disorder by diffracting around it. In particular, our analysis of monolayer graphene yields a mode damping that quickly vanishes at long electron wavelengths near charge neutrality, scaling as $\gamma(k) \sim k^2$
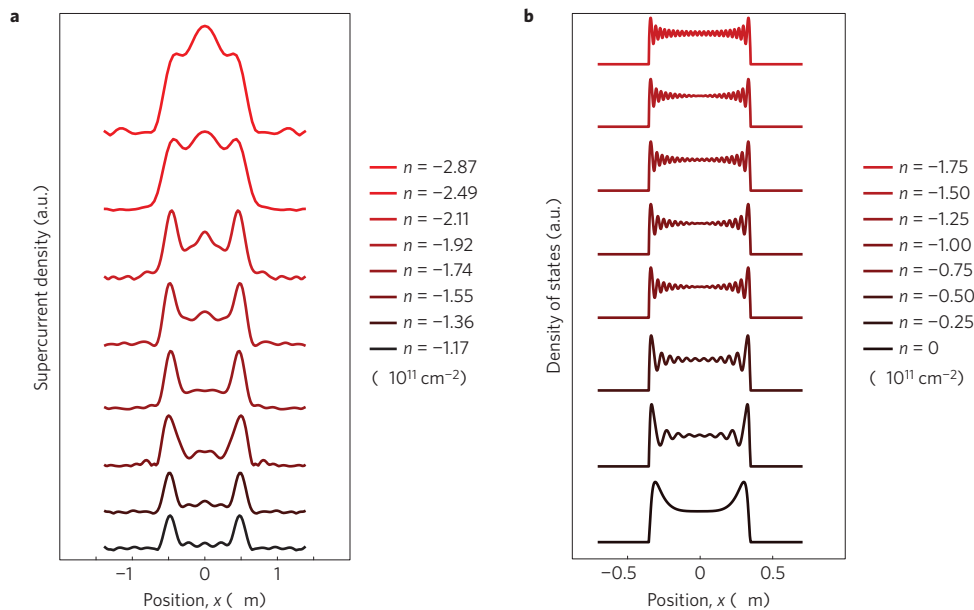
Figure 4 | 'Fibre-optic' theoretical model of transport in graphene. a, Real-space maps of measured current flow $J(x)$ in bilayer device $BL3$ at fixed carrier densities on the hole side, showing edge currents near the Dirac point and a continuous evolution towards bulk flow. **b**, Theoretical plot of spatially resolved density of states in bilayer graphene at fixed carrier densities for the edge waveguide model. For the simulation, an effective delta function potential approximation is used with the best-fit value $\hbar u = 0.7$ eV nm and the Fermi wavelength values in each case corresponding to the density values (see Supplementary Information). The band mass of bilayer graphene is taken as $0.028 m_e$, where m_e is the electron mass.

(see Supplementary Methods). This resembles the behaviour of optical guided states in so-called 'weakly guiding' optical fibres, where a similar suppression of disorder scattering occurs due to evanescent waves diffracting around edge disorder.

One appealing aspect of the fibre-optic model is that it can naturally accommodate a wide range of different microscopic physical mechanisms discussed theoretically in the literature[27–31] that may produce an edge potential. Examples include pinning of the Fermi energy to the low-energy states due to broken A/B sublattice symmetry[29–31], density accumulation caused by dangling bonds or trapped charges at the boundaries, or electrostatics[27,28]. The competition of these effects can produce a complex dependence of the edge potential $V(x)$ on carrier density. Pinpointing the precise microscopic origins of the edge potential requires further study.

To the best of our knowledge, the fibre-optic modes is perhaps the simplest model fully consistent with the observations. In particular, we eliminate edge density accumulation, which can influence the edge potential and in principle also support guided edge currents. The fact that the charge neutrality points for both edge and bulk roughly coincide in density n suggests an absence of a positional charge imbalance on a large scale (Fig. 2f). In addition, edge-dominated current flow is observed near the Dirac point, but not at higher densities, behaviour not expected for strong edge doping. Explanations involving electron–hole puddles are excluded by the reproducibility of edge currents with widths of the order of the electron wavelength across many samples, as well as the observation that edge currents tend to be stronger in clean samples with ballistic Fabry–Pérot interference[32] (see Supplementary Fig. 6 for normal state characterization of the graphene). Large charge inhomogeneities across the sample would suppress Fabry–Pérot interference and are thus unlikely.

Lastly, it is widely known that the A/B sublattice imbalance for broken bonds at the edge can lead to edge modes in pristine graphene at neutrality. Such dispersing zero-mode states can exist even in the absence of a line potential, forming edge modes for an atomically perfect zigzag edge[29–31]. However, our simulations for a disordered edge show that these states are highly localized

on the disorder length scale, and also that edge roughness induces strong scattering between the states at the boundary and in the bulk, which hinders ballistic propagation. Similarly, valley Hall currents predicted at the boundaries of a gapped bilayer due to momentum-space Berry curvature of the bands[33,34] are eliminated because they are highly sensitive to disorder scattering at the boundaries.

Our measurements establish that edge currents are present in graphene even at zero magnetic field, near the Dirac point. The observed edge currents are linked to electronic guided-wave states formed owing to band bending at the edge. This demonstrates confinement of electron waves at a level comparable to that for light in photonic systems and defines a new mode for the transmission of electronic signals at the nanoscale. We anticipate this work will inspire more detailed investigations of boundary states in graphene and other materials. Such capabilities are also of great interest owing to the predicted topological nature of edge states along stacking domain boundaries in bilayer graphene[35,36].

References

1. Castro Neto, A. H., Guinea, F., Peres, N. M. R., Novoselov, K. S. & Geim, A. K. The electronic properties of graphene. *Rev. Mod. Phys.* **81**, 109–162 (2009).
2. Katsnelson, M. I., Novoselov, K. S. & Geim, A. K. Chiral tunnelling and the Klein paradox in graphene. *Nature Phys.* **2**, 620–625 (2006).
3. Young, A. F. & Kim, P. Quantum interference and Klein tunnelling in graphene heterojunctions. *Nature Phys.* **5**, 222–226 (2009).
4. Campos, L. *et al.* Quantum and classical confinement of resonant states in a trilayer graphene Fabry–Perot interferometer. *Nature Commun.* **3**, 1239 (2012).
5. Varlet, A. *et al.* Fabry–Pérot interference in gapped bilayer graphene with broken anti-Klein tunneling. *Phys. Rev. Lett.* **113**, 116601 (2014).
6. Cheianov, V. V., Fal'ko, V. & Altshuler, B. L. The focusing of electron flow and a Veselago lens in graphene p–n junctions. *Science* **315**, 1252–1255 (2007).
7. Shytov, A. V., Rudner, M. S. & Levitov, L. S. Klein backscattering and Fabry–Perot interference in graphene heterojunctions. *Phys. Rev. Lett.* **101**, 156804 (2008).
8. Mayorov, A. S. *et al.* Micrometer-scale ballistic transport in encapsulated graphene at room temperature. *Nano Lett.* **11**, 2396–2399 (2011).

9. Pereira, J. M., Mlinar, V., Peeters, F. M. & Vasilopoulos, P. Confined states and direction-dependent transmission in graphene quantum wells. *Phys. Rev. B* **74,** 045424 (2006).
10. Zhang, F.-M., He, Y. & Chen, X. Guided modes in graphene waveguides. *Appl. Phys. Lett.* **94,** 212105 (2009).
11. Hartmann, R. R., Robinson, N. J & Portnoi, M. E. Smooth electron waveguides in graphene. *Phys. Rev. B* **81,** 245431 (2010).
12. Williams, J. R., Low, T., Lundstrom, M. S. & Marcus, C. M. Gate-controlled guiding of electrons in graphene. *Nature Nanotech.* **6,** 222–225 (2011).
13. Dynes, R. C. & Fulton, T. A. Supercurrent density distribution in Josephson junctions. *Phys. Rev. B* **3,** 3015–3023 (1971).
14. Taychatanapat, T., Watanabe, K., Taniguchi, T. & Jarillo-Herrero, P. Electrically tunable transverse magnetic focusing in graphene. *Nature Phys.* **9,** 225–229 (2013).
15. Ritter, K. A. & Lyding, J. W. The influence of edge structure on the electronic properties of graphene quantum dots and nanoribbons. *Nature Mater.* **8,** 235–242 (2009).
16. Tao, C. *et al.* Spatially resolving edge states of chiral graphene nanoribbons. *Nature Phys.* **7,** 616–620 (2011).
17. Oostinga, J. B., Heersche, H. B., Liu, X., Morpurgo, A. F. & Vandersypen, L. M. K. Gate-induced insulating state in bilayer graphene devices. *Nature Mater.* **7,** 151–157 (2007).
18. Bischoff, D., Libisch, F., Burgdrfer, J., Ihn, T. & Ensslin, K. Characterizing wave functions in graphene nanodevices: Electronic transport through ultrashort graphene constrictions on a boron nitride substrate. *Phys. Rev. B* **90,** 115405 (2014).
19. Barone, A. & Paterno, G. *Physics and Applications of the Josephson Effect* (John Wiley, 1982).
20. Dean, C. R. *et al.* Boron nitride substrates for high-quality graphene electronics. *Nature Nanotech.* **5,** 722–726 (2010).
21. Tinkham, M. *Introduction to Superconductivity* (McGraw-Hill, 1975).
22. Cuevas, J. C. & Bergeret, F. S. Magnetic interference patterns and vortices in diffusive SNS junctions. *Phys. Rev. Lett.* **99,** 217002 (2007).
23. Hui, H.-Y., Lobos, A. M., Sau, J. D. & Sarma, S. Das Proximity-induced superconductivity and Josephson critical current in quantum spin Hall systems. *Phys. Rev. B* **90,** 224517 (2014).
24. Jaklevic, R. C., Lambe, J. & Mercereau, J. E. Quantum interference effects in Josephson tunneling. *Phys. Rev. Lett.* **12,** 159–160 (1964).
25. McCann, E. Asymmetry gap in the electronic band structure of bilayer graphene. *Phys. Rev. B* **74,** 161403 (2006).
26. Castro, E. V. *et al.* Biased bilayer graphene: Semiconductor with a gap tunable by the electric field effect. *Phys. Rev. Lett.* **99,** 216802 (2007).
27. Jackiw, R. & Rebbi, C. Solitons with fermion number. *Phys. Rev. D* **13,** 3398–3409 (1976).
28. Silvestrov, P. G. & Efetov, K. B. Charge accumulation at the boundaries of a graphene strip induced by a gate voltage: Electrostatic approach. *Phys. Rev. B* **77,** 155436 (2008).
29. Nakada, K., Fujita, M., Dresselhaus, G. & Dresselhaus, M. S. Edge state in graphene ribbons: Nanometer size effect and edge shape dependence. *Phys. Rev. B* **54,** 17954–17961 (1996).
30. Akhmerov, A. R. & Beenakker, C. W. J. Boundary conditions for Dirac fermions on a terminated honeycomb lattice. *Phys. Rev. B* **77,** 085423 (2008).
31. Castro, E. V., Peres, N. M. R., dos Santos, J. M. B. L., Neto, A. H. C. & Guinea, F. Localized states at zigzag edges of bilayer graphene. *Phys. Rev. Lett.* **100,** 026802 (2008).
32. Allen, M. T. *et al.* Visualization of phase-coherent electron interference in a ballistic graphene josephson junction. Preprint at http://arxiv.org/abs/1506.06734 (2015).
33. Xiao, D., Yao, W. & Niu, Q. Valley-contrasting physics in graphene: Magnetic moment and topological transport. *Phys. Rev. Lett.* **99,** 236809 (2007).
34. Jung, J., Zhang, F., Qiao, Z. & MacDonald, A. H. Valley-Hall kink and edge states in multilayer graphene. *Phys. Rev. B* **84,** 075418 (2011).
35. Zhang, F., MacDonald, A. H. & Mele, E. J. Valley Chern numbers and boundary modes in gapped bilayer graphene. *Proc. Natl Acad. Sci. USA* **110,** 10546–10551 (2013).
36. Alden, J. S. *et al.* Strain solitons and topological defects in bilayer graphene. *Proc. Natl Acad. Sci. USA* **110,** 11256–11260 (2013).

Author contributions
M.T.A. and A.Y. designed and fabricated the devices, performed the experiments, analysed the data, and wrote the paper. O.S. and L.S.L. developed the theoretical model of guided edge modes and wrote the paper. A.R.A. and I.C.F. performed the Bayesian analysis of the Fraunhofer patterns. P.J.-H. contributed to discussions of the results and wrote the paper. K.W. and T.T. provided the hexagonal boron nitride crystals used in device fabrication.

Additional information
Supplementary information is available in the online version of the paper. Reprints and permissions information is available online at www.nature.com/reprints. Correspondence and requests for materials should be addressed to A.Y.

Competing financial interests
The authors declare no competing financial interests.